IEEE Access
Multidisciplinary ⋮ Rapid Review ⋮ Open Access Journal

Received 20 April 2024, accepted 4 May 2024, date of publication 8 May 2024, date of current version 15 May 2024.

Digital Object Identifier 10.1109/ACCESS.2024.3398144

RESEARCH ARTICLE

Ultrathin Single Layer Transmissive Dual-Band Linear to Circular Converter for Non-Adjacent Dual Orthogonal Circularly Polarized Antenna

SOUMIK DEY, (Graduate Student Member, IEEE), AND SUKOMAL DEY, (Senior Member, IEEE)
Department of Electrical Engineering, Indian Institute of Technology Palakkad, Kanjikode, Kerala 678623, India

Corresponding author: Sukomal Dey (sukomal.iitpkd@gmail.com)

This work was supported in part by the Science and Engineering Research Board, Government of India, under Project TTR/2022/000001; and in part by the 2023 IEEE Antennas and Propagation Society Fellowship.

ABSTRACT This paper presents a new dual-band transmissive type linear to circular polarizer (LTCP) on a single-layer ultra-thin dielectric substrate. The unit cell of the converter consists of dual circular split rings and a connected cross-grid dipole at the center, for which the metal layer is engraved on a 0.51 mm thick Taconic TLY-5 substrate. The converter rotates the polarization of the incident linearly polarized (LP) wave into single circularly polarized (CP) transmitted waves at two non-adjacent bands, X and K. The LTCP exhibits oblique angle stability up to 35° with independent controllable frequencies at 11.2 / 22.75 GHz. A prototype of the LTCP is fabricated, and the LP to CP conversion is measured to be between 10-12.54 GHz (22.5 %) and 21.82-24.57 GHz (11.8 %) with a corresponding axial ratio (AR) below 3 dB. The experimental results of the converter confer well with the simulation results at normal and oblique incidences. The size of the designed converter is $0.2 \times 0.2 \times 0.019\ \lambda_L^3$, where λ_L is the wavelength at the center frequency of the lower band. The dual-feed LP stacked radiating patch is integrated with the LTCP to realize dual-band dual orthogonal (RCP/LCP) CP microstrip antenna (CPMA). The shared ground is strategically conceived in designing the dual-feed LP antenna, in which the bottom metal layer serves as a ground plane in the lower band and as a reflector in the higher band to provide broadside radiation. The simulation and measured results validate the design principle of the recommended dual-band dual CPMA.

INDEX TERMS Axial ratio, circularly polarized antenna, dual-band antenna, linear to circular polarization converter, metasurface, multilayer stacked geometry, shared ground plane.

I. INTRODUCTION

Polarization of the antenna imposes notable importance for satellite communication (SatCom), WiMAX, WLAN, and global positioning system (GPS) [1]. In such cases, the circularly polarized (CP) antenna gains importance over the linearly polarized (LP) antenna because of countervailing the polarization rotation (known as Faraday rotation) in the atmosphere and withstanding the polarization mismatch between transmitter and receiver. For polarimetric synthetic aperture radar (SAR), the CP antenna has advantages over dual-orthogonal LP antennas in reconstructing reflectivity images [2]. SAR is utilized in non-destructive testing, security imaging and biomedical imaging by combining backscattered microwave signals to image the target. For detecting cracks inside metallic objects, CP SAR can easily identify the relative orientation of the target by analyzing the polarization angle. In space-borne SAR, the LP antenna is replaced with a CP one to avoid polarization impairment in the receiver stage and degradation of SAR image quality [3]. Traditional design of CP microstrip antennas (CPMA) using single feed face challenges because of narrow 3 dB AR bandwidth (BW). Instead, the dual-feed or multi-feed is adopted to realize the CPMA for broadband wireless

The associate editor coordinating the review of this manuscript and approving it for publication was Shah Nawaz Burokur.

communication. In single-feed techniques, antenna arrays with driven and parasitic patches are used for obtaining wide-band CP BW [4], [5], [6]. Different topologies are realized for the feeding network based on sequential phase variation, series-parallel stub, Wilkinson power divider, and broad-band balun to improve the AR BW at the expense of large spacing and design complexity [7], [8], [9]. In some designs, the absence of a full ground plane may degrade the radiation performance if the antenna is mounted on a metal platform [10]. The cross dipole antenna backed with a reflector has been proposed for wideband CPMA with uni-directional radiation, but the antenna requires a minimum profile height of $\sim \lambda$ /4 at the lowest frequency of operation [11]. The uplink/downlink frequencies in SatCom, polarimetric SAR, multiband GPS and wireless systems demand dual broadband CP antenna, which is rarely achieved using the above complex feeding methods. A dual-band CP patch antenna adopting a shared aperture was proposed with sequential phase excitation, but the non-planar geometry is unsuitable for monolithic integration [12]. The other dual-band CPMAs usually possess narrow AR BW and exhibit low gain [13], [14], [15]. Another method of implementing the CPMA that has become popular recently is based on the chiral metamaterial resonant structure. Two dimensional (2D) periodic arrangement of metamaterial unit cells known as metasurface exhibits un-usual properties like negative refractive index, reversal of Snell's law, reversal of Doppler effect etc. The metasurface can be engineered into 2D anisotropic geometry to manipulate the polarization of the incident electromagnetic (EM) wave within the frequency-selective operating band in microwave and optical ranges. Different frequency selective surface (FSS) based linear to circular polarizers (LTCPs) are reported. They can be classified into two kinds- reflective type [16], [17], [18], [19], [20] and transmissive type [21], [22], [23], [24], [25], [26], [27], [28], [29], [30], [31], [32], [33], [34], [35]. Despite reflective-type LTCPs exhibiting wideband operation and high conversion efficiency, the blockage from the antenna feed affects the CP radiation. Instead, transmissive-type converters seem much more attractive, but their operation is limited by narrow AR BW and high insertion loss (IL). Multilayer geometry has been adopted to overcome the limitation of single-layer converters. Dual-layer structure based on the Jerusalem cross element was conceived for LTCP with wide-angle stability [22]. An extremely wide-band polarizer consisting of four FSS layers is proposed to convert an LP wave into a CP wave between 5.75-11.2 GHz (64.3 %) [23]. However, the structure shows a stable AR response up to an incidence angle of 20°. A third-order FSS is employed to design an LP-to-CP converter in the X-band but with a low AR BW and higher profile height [24]. Apart from multi-layer geometry, different wideband LTCPs are realized on a single substrate, significantly reducing the complexity [25], [26], [27]. Multi-channel communication system motivates designing dual-band transmissive type LP-to-CP converters on a single layer and multilayer configuration [28], [29], [30], [31], [32], [33], [34], [35]. Usually, in single-layer LTCP, identical FSS with asymmetric periodic patterns are printed on both sides of the substrate. As mentioned in [31], it is challenging to design an LTCP with dual broadband operation, high angle stability, and low IL on a thin dielectric substrate. Recently phase-changing materials (PCMs) like-vanadium dioxide and graphene were used to design tunable linear-to-cross converter and LTCP [36], [37]. Even though the operations of these PCMs are very attractive, especially at the terahertz (THz) and optical frequencies, but precise controls of the transition temperature, chemical potential, and dielectric permittivity are required. Developing a frequency tunable LTCP at microwave/millimeter wave regime using active switches (PIN diode, varactor) remains a challenging task. One can not ignore the additional losses from the switching elements, especially for transmissive type converter, and its performance degradation due to the biasing circuit of the active elements. Except for the LTCP in [31], the previous designs of dual-band converters rarely show independent control of two operating frequencies relative to changes in geometrical parameters. Also, frequency tuning of the dual-band LTCP in [31] was presented over a narrow frequency range, which may have limited use in practical scenarios. The dual orthogonal circular rotation in [28], [29], [30], [31], [32], and [33] imposes a stringent condition on the LP antenna (LPA) feed with the same polarization at dual frequencies. However, a dual-band LPA with dual orthogonal feed is more advantageous, considering two non-adjacent resonant frequencies and high isolation between the ports [38]. The LTCP needs to be designed with the same polarization at dual-band to integrate with dual-orthogonal feed LPA.

This paper proposes a single-layer dual-band LTCP with similar polarization rotation characteristics at two non-adjacent bands, X and K. The polarizer exhibits broadband LP-to-CP conversion with measured AR $\leq$ 3 dB BWs of 22.5 and 11.8 %. The unique contributions of the present works are (a) the independent control of the two LP-to-CP conversion bands by adjusting the geometrical parameters, providing wide tuning ranges of 1.9 and 1.7 GHz for the center frequencies (b) broadband AR BW at dual LP to CP conversion frequencies with a high oblique angle stability of 35°, (c) developing a new dual-band dual-feed LPA (DF-LPA) using strategic incorporation of the shared ground plane with stacked radiating patches to realize dual-band dual-orthogonal CPMA.

The proposed metasurface is placed as a superstrate over DF-LPA to transform the linear polarization into circular polarization. The present work is different to that in [39], in which the metasurface is placed as a superstrate in the near-filed region of a microstrip antenna to reduce the mutual coupling between H-plane coupled multiple input multiple output array. Also, the low correlation due to the orthogonal coupling mode transformation was presented over a single band; whereas the proposed metasurface transforms the far-field radiation of the DF-LPA into CP radiation at

two distinct frequencies. The CPMA exhibits broad AR BWs of 5.4 and 2.8 % in the two bands, with a peak gain of 8.4 and 6.4 dBic, respectively. High isolation of > 20 dB between the two feeding ports of CPMA will ensure low interference between uplink/downlink communication channels. Section II describes the geometry of the proposed LTCP and its working principle based on equivalent circuit and full wave simulation. The experimental results of the converter are discussed in section III. Section IV presents the simulation and measurement results of the converter-loaded dual-band dual-orthogonal CPMA.

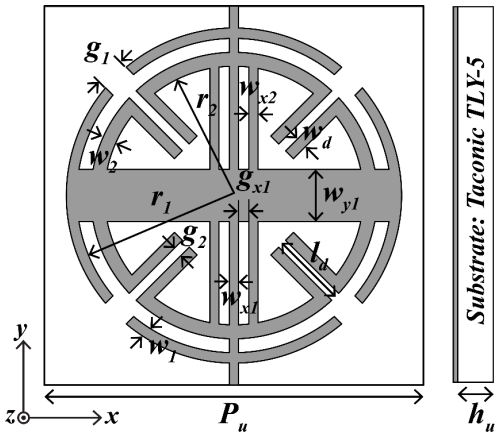

FIGURE 1. Unit cell geometry of the transmissive type linear to circular converter.

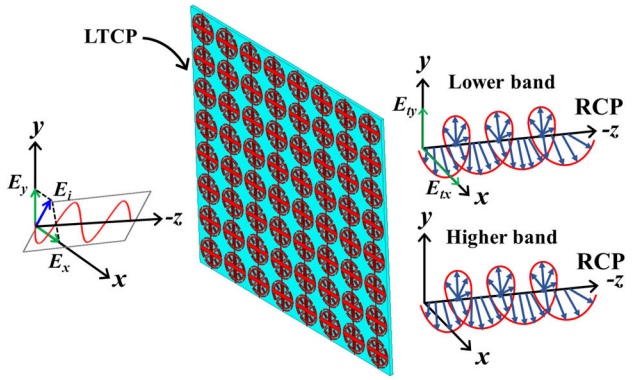

FIGURE 2. Working principle of the polarization converter that converts linear polarized wave into the right circularly polarized wave in dual frequencies.

II. DESIGN OF DUAL-BAND LTCP

A. UNIT CELL DESCRIPTION

Fig. 1. shows the layout of the dual-band LTCP, which is modelled on Taconic TLY-5 substrate (relative permittivity $\varepsilon_r = 2.2$, loss tangent $tan\ \delta = 0.0009$). The converter has a periodic pattern of dual circular split rings (CSRs) geometry. Four split gaps are incorporated in each circular ring along the diagonals of the unit cell. The splits are rotated by an angle of ±45° and ±135° considering an angular separation of 90°

TABLE 1. Dimensions of the linear to circular polarizer in millimeter.

P_u	h_u	r_1	w_1	g_1	r_2	w_2
5.45	0.51	2.26	0.15	0.42	1.86	0.2
g_2	l_d	w_d	w_{x1}	w_{x2}	g_{x1}	w_{y1}
0.14	1.1	0.16	0.13	0.13	0.15	0.75

between them. For the inner circular ring, a pair of parallel strips (having width = w_d and length = l_d) are attached on two sides of each split gap. This enhances additional capacitance loading to the structure, causing an increase in the effective resonating length [40]. The CSRs are connected at the center by a cross dipole resonator (CDR) having different widths of w_{y1} and w_{x1} for the horizontal and vertical arms. The vertical arm of the CDR is extended across the unit cell's boundary edges, which will make a wire metal grid in a periodic 2D array geometry. Two vertical metal strips of width w_{x2} are symmetrically placed on each side of the wire grid to control the phase difference between the x and y-polarized transmitted waves. The unit cell has a periodicity (P_u) of 5.45 mm, which is approximately 0.2 λ_L at the lowest operating frequency of the converter.

B. OPERATING PRINCIPLE

The anisotropic geometry of the designed unit cell provides different transmission responses along the x and y polarization directions. Fig. 2 presents the schematic of the circular polarizer to describe the design topology under LP plane wave incidence. The converter is illuminated with an EM wave with the electric field slanted at an angle of 45° to the x and y axes. The overall incident field ($\vec{E}_i$) can be decomposed into two orthogonal components given in (1)

$$\vec{E}_i = 1\Big/\sqrt{2}\left(\hat{x}E_x + \hat{y}E_y\right) \tag{1}$$

The converter exhibits different transmission bands for $x$and y polarization having corresponding transmission coefficients' (T_{xx} and T_{yy}) magnitudes are > −3 dB. The transmitted signals (E_t) are calculated using (2)

$$\vec{E}_{tx} = \hat{x}T_{xx}E_x \ \text{ and } \ \vec{E}_{ty} = \hat{y}T_{yy}E_y \tag{2}$$

The equation (2) assumes negligible mutual coupling between two orthogonal transmitted signals, i.e. $T_{xy} = T_{yx} = 0$. This assumption has been made due to the connected cross-dipole geometry at the center of the proposed unit cell [22]. The transmitted wave will be circularly polarized if magnitudes of two co-polarized transmission coefficients are nearly equal, with quadrature phase differences between them. For dual-band LTCP, (3) needs to be satisfied at two distinct frequencies according to the above discussion.

$$|T_{xx}| = |T_{yy}| \text{ and } \phi_{xx} = \phi_{yy} \pm 90° \tag{3}$$

where $T_{xx} = |T_{xx}|e^{j\phi_{xx}}$ and $T_{yy} = |T_{yy}|e^{j\phi_{yy}}$. When $\Delta\phi = -90°$ the transmitted wave is right circularly polarized

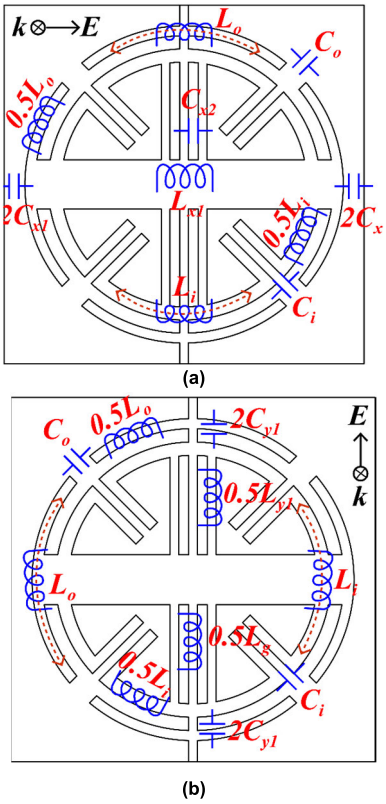

FIGURE 3. Inductive and capacitive components of the proposed dual-band LTCP (a) x-polarized incidence (b) y-polarized incidence.

(RCP), whereas when $\Delta\phi = +90°$ the wave is left circularly polarized (LCP). The full-wave analysis of the converter was executed using the Ansys High Frequency Structure Simulator (HFSS) of ver. 2020. Table 1 renders the final design parameters of the unit cell. The minimum width of the metal lines and the gap between the adjacent lines are fixed at 0.13 mm, depending on the fabrication tolerance.

C. EQUIVALENT CIRCUIT MODEL

Fig. 3 presents the inductive and capacitive components of the different constituent parts of the unit cell for x-polarized and y-polarized incidence. When the electric field of the incident EM signal is parallel to the edges of the circular ring, a surface current will induce along the length of the circular arc, and it is modelled as an inductance. Each split gap in a circular ring is modelled as a capacitance. Fig. 4 displays the equivalent circuits of the designed converter for x and y-polarized incident waves. The outer and inner CSRs are modelled as inductors (L_o and L_i) and capacitors (C_o and C_i) in series. The inductances (L_j) of the ring can be obtained from (4) [41]

$$L_j = K_j\mu_0(r_j + 0.5w_j) \times \left[\log\left(1 + \frac{2r_j}{w_j}\right) + 0.9 + 0.2\left(1 + \frac{2r_j}{w_j}\right)^{-2}\right] \quad (4)$$

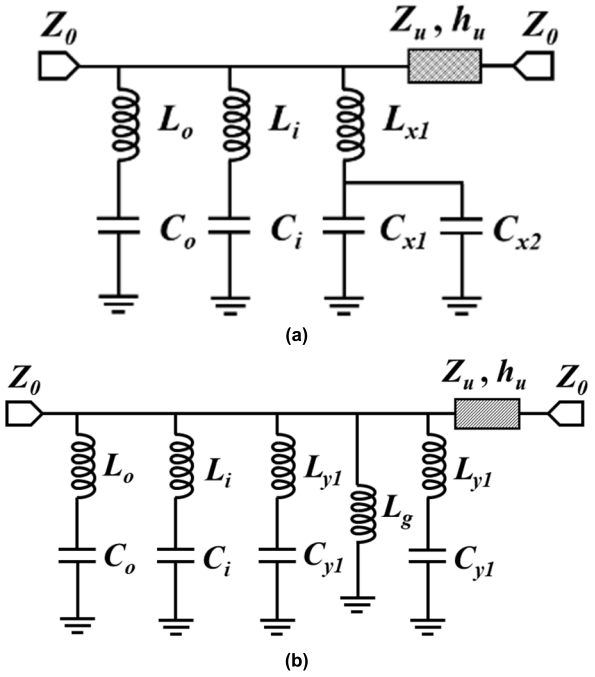

FIGURE 4. Equivalent circuit of the converter (a) x-polarization (b) y-polarization.

TABLE 2. Circuit parameters for the equivalent circuit of LTCP.

Initial Values From The Analytical Model				
L_o (nH)	L_i (nH)	L_{x1} (nH)	L_{y1} (nH)	L_g (nH)
6.19	5.14	1.51	2.79	1.55
C_o (fF)	C_i (fF)	C_{x1} (fF)	C_{x2} (fF)	C_{y1} (fF)
10.98	13.6	5.68	4.9	0.66
Optimized Values From Curve Fitting				
L_o (nH)	L_i (nH)	L_{x1} (nH)	L_{y1} (nH)	L_g (nH)
9.78 (x-pol) / 5.86 (y-pol)	7.77	1.45	1.54	1.71
C_o (fF)	C_i (fF)	C_{x1} (fF)	C_{x2} (fF)	C_{y1} (fF)
13.07 (x-pol) / 10.31 (y-pol)	13.1	10.09	7.86	8.1

Here, values of K_j for the outer and inner rings are (1-$2g_1/\pi r_1$) and (1-$2g_2/\pi r_2$), respectively. The capacitance (C_j) associated with the ring can be written as an addition of gap capacitance $\left(C_g^j\right)$ and surface capacitance $\left(C_s^j\right)$ [41]. So, $C_j = C_g^j + C_s^j$. Where,

$$C_g^j = \varepsilon_0\varepsilon_{eff}\left[\left(tw_j/g_j\right) + t + w_j + g_j\right] \quad (5)$$

$$C_s^j = \frac{2\varepsilon_0\varepsilon_{eff}\left(t + w_j\right)}{\pi}\log\left(\frac{4r_j + 2w_j}{g_j}\right) \quad (6)$$

The $\varepsilon_{eff} = 0.5\left(1 + \varepsilon_r\right)$ is the effective dielectric constant of the substrate and t is the thickness of the copper whose value is 0.035 mm. For the inner circular ring, an additional term $\varepsilon_0\varepsilon_{eff}\left(l_d t/g_2\right)$is added to the gap capacitance $\left(C_g^2\right)$ in (5) to account for parallel diagonal strips attaching to each

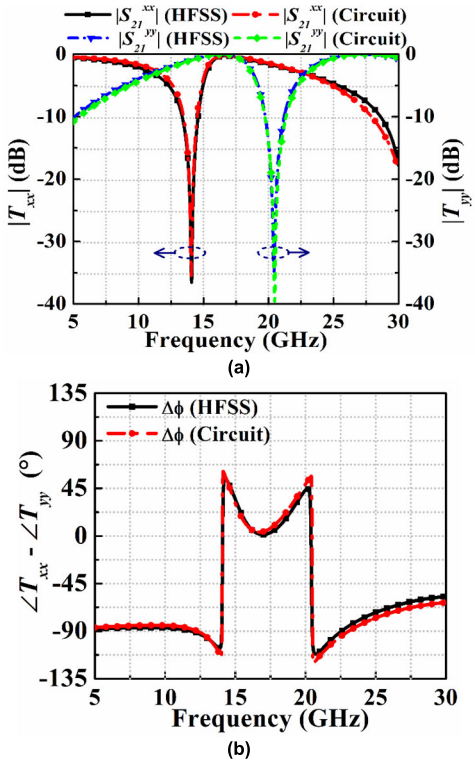

FIGURE 5. Simulated transmission coefficients obtained from full wave simulation and circuit simulation (a) magnitude of S_{21} for x and y-polarized incidences (b) phase difference between T_{xx} and T_{yy}.

split gap. The connected cross dipole at the center of the circular rings will resonate when the electric field is parallel to the dipole arm. The wide metal strip along the x-axis is modelled using a series L-C resonator (L_{x1} and C_{x1}). An additional capacitance, C_{x2} is placed in parallel to C_{x1} to account for the capacitance that arises from the pair of parallel strips along the y-axis. Similarly, for y-polarized incidence, the pair of vertical strips on both sides of the center wire grid provides a series resonant circuit L_{y1}- C_{y1}. The self-inductance of a metal strip of length $= l_m$, width $= w_m$ and thickness $= t$ is given by (7) [31]

$$L_m = \frac{\mu_0}{2\pi} l_m \left(0.57 - 0.145 \ln \frac{w_m}{h_u}\right) \left[\ln\left(\frac{l_m}{w_m + t}\right) + 1.193 + 0.2235\left(\frac{w_m + t}{l_m}\right)\right] \quad (7)$$

For L_{x1} and L_{y1}, the values of l_m are replaced with $2(r_1 + w_1)$ and $2(r_2 + w_2)$, whereas the values of w_m are replaced with w_{y1} and w_{x2}, respectively. For a periodic geometry of rectangular metallic strip, capacitance C_m between adjacent unit cells is obtained using (8) [42]

$$C_m = \varepsilon_0 \varepsilon_{eff} K_m \frac{2P_u}{\pi} \log\left\{\frac{1}{\sin\left(\pi S_m / 2P_u\right)}\right\} \quad (8)$$

Here K_m is the correction factor whose values are $w_{y1}/2(r_1+w_1)$ and w_{x2} / $2(r_2+ w_2)$ for the capacitance C_{x1} and C_{y1}. In (8), the S_m is replaced with $[P_u$ - $2(r_1 + w_1)]$ and $[P_u$- $2(r_2 + w_2)]$ while determining the inter-element capacitances for x and y-polarized waves. The self-inductance of the metal wire grid along the y-axis is calculated using (9) [42]

$$L_g = \mu_0 \frac{P_u}{2\pi} \log\left(\sin \frac{\pi w_{x1}}{2P_u}\right)^{-1} \quad (9)$$

One can find the capacitance C_{x2} using the parallel plate capacitor equation as given in (10)

$$C_{x2} = \varepsilon_0 \varepsilon_{eff} (r_2 - 0.5 w_{y1}) t g_{x1}^{-1} \quad (10)$$

In (4)-(10) ε_0 and μ_0 denote the permittivity and permeability of the EM signal in free space. In the recommended equivalent circuit, a short transmission line (characteristic impedance of $Z_u = Z_0/\sqrt{\varepsilon_r} = 254.2\Omega$ and length of $h_u = 0.51$ mm) denotes the dielectric substrate. Here, $Z_0 = 120\pi$ is the wave impedance of free space. The above equations can be considered as a design guideline for implementing LTCP. The values of circuit parameters, as calculated from analytical expressions, are listed in Table 2. The circuit simulation of the converter was performed using Advanced Design System (ADS) software of ver. 2020. The transmission coefficients in circuit simulation are matched with the full-wave simulation response by slightly tuning the L-C parameters for x and y-polarized incidence. The values of L_0 and C_0 are chosen differently for TE and TM polarizations to account for the unequal mutual inductances along x and y-axes. Table 2 also presents the optimum values of the circuit parameter.

D. SIMULATION RESULTS

The unit cell in Fig. 1 is simulated using periodic boundaries along x and y directions with a plane wave excitation using Floquet ports. Fig. 5(a) presents the simulated co-polarized transmission coefficient ($|S_{21}|$) of the converter at normal incidence. In the case of x-polarized incidence, the polarizer shows a transmission zero (TZ) at 13.85 GHz, having passbands on both sides with $|S_{21}| \geq -3$ dB. Similarly, for the y-incident wave, the polarizer exhibits TZ at 20.05 GHz. At 11.2 and 22.75 GHz $\left|S_{21}^{xx}\right| \approx \left|S_{21}^{yy}\right|$, with transmission magnitudes are ~ -2.9 dB, respectively. This meets the amplitude criterion of (3). Fig. 5(b) shows the phase difference between two orthogonal transmission coefficients, which is near $-90°$, causing RCP transmitted wave. Fig. 5 also includes the response of the circuit model for both polarizations, with a close resemblance observed with that of the full wave simulation. The axial ratio (AR) is commonly used to illustrate the performance of the linear to circular converter. The AR is related to the T_{xx} and T_{yy} using the relation given by (11) [31]

$$AR = \sqrt{\frac{|T_{xx}|^2 + |T_{yy}|^2 + \sqrt{a}}{|T_{xx}|^2 + |T_{yy}|^2 - \sqrt{a}}} \quad (11)$$

where, $a = |T_{xx}|^4 + |T_{yy}|^4 + 2|T_{xx}|^2 |T_{yy}|^2 \cos(2\Delta\phi)$ and $\Delta\phi = \phi_{xx} - \phi_{yy}$. Fig. 6 shows the AR of the converter as obtained from circuit simulation and EM simulation. The

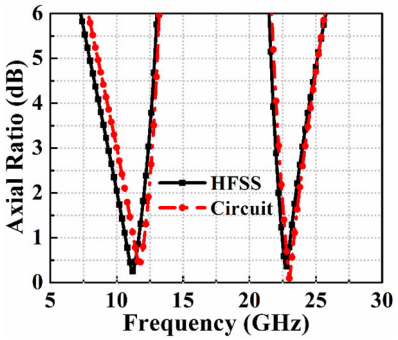

FIGURE 6. Simulated axial ratio of the designed dual-band converter.

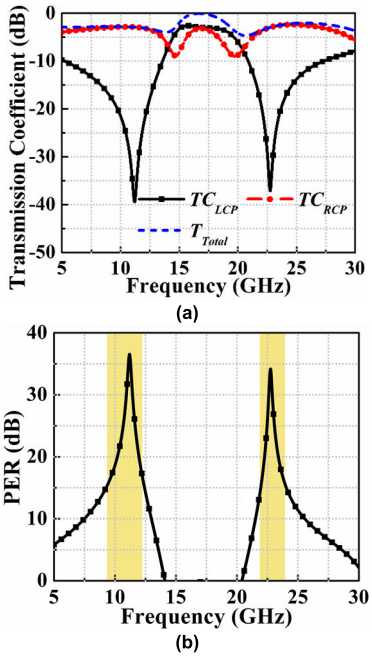

FIGURE 7. Simulated (a) linear to circular transmission coefficients and total transmission coefficient (b) PER at normal incidence.

minima of ARs at two center frequencies are obtained as 0.25 and 0.33 dB. The AR $\leq$ 3 dB BW of the converter is achieved between 9.36 to 12.39 GHz (27.9 %) and 21.98 to 23.98 GHz (8.7 %). The linear to circular transmission coefficients (TC) are obtained separately for LCP and RCP, as given in (12), [31]

$$TC_{LCP} = \left(T_{xx} + jT_{yy}\right)/2 \text{ and } TC_{RCP} = \left(T_{xx} - jT_{yy}\right)/2 \tag{12}$$

The total IL of the polarizer is calculated using (13) [44]

$$T_{Total} = \sqrt{\left(|T_{xx}|^2 + |T_{yy}|^2\right)/2} \tag{13}$$

For the designed LTCP, magnitudes of TC_{LCP}, TC_{RCP}, and T_{Total} are shown in Fig. 7 (a). The converter transforms an LP wave into RCP at lower and higher frequencies with ILs of $<$ 2.91 and $<$ 2.96 dB, respectively. A term called polarization extinction ratio (PER) is defined as the ratio

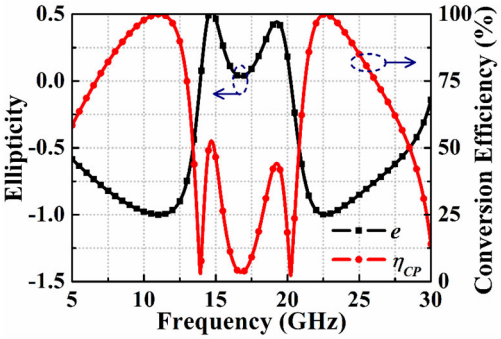

FIGURE 8. Simulated ellipticity and conversion efficiency of the LTCP.

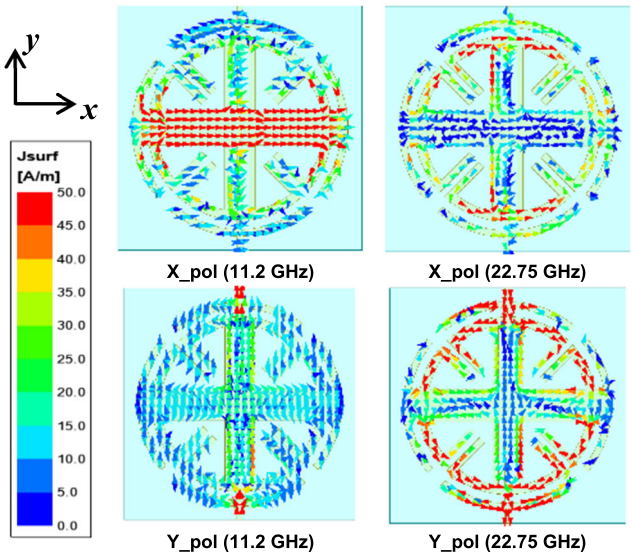

FIGURE 9. Surface current on LTCP at center frequencies of AR band.

of co-circular transmission to cross-circular transmission, as presented in Fig. 7(b). The PER is achieved to be $>$ 36.7 dB at 11.2 GHz and $>$ 34.5 dB at 22.75 GHz.

E. STOKES PARAMETERS AND ENERGY CONVERSION EFFICIENCY

To validate the operating principle of the LTCP, the ellipticity (e) is evaluated from the Stokes parameters using (14)-(15) [43]

$$I = |T_{xx}|^2 + |T_{yy}|^2 \text{ and } Q = |T_{xx}|^2 - |T_{yy}|^2 \tag{14}$$

$$U = 2\,|T_{xx}|\,|T_{yy}|\cos\Delta\phi \text{ and } V = 2\,|T_{xx}|\,|T_{yy}|\sin\Delta\phi \tag{15}$$

The ellipticity of the converter is defined as $e = V/I$, whose value is '+1' for LCP and '−1' for RCP. Fig. 8 presents the ellipticity of the designed converter, confirming transmitted wave is RCP at both frequencies. The LP to CP conversion efficiency (η_{CP}) is defined as (16) [27]

$$\eta_{CP} = \frac{\left||TC_{RCP}|^2 - |TC_{LCP}|^2\right|}{|TC_{RCP}|^2 + |TC_{LCP}|^2} \tag{16}$$

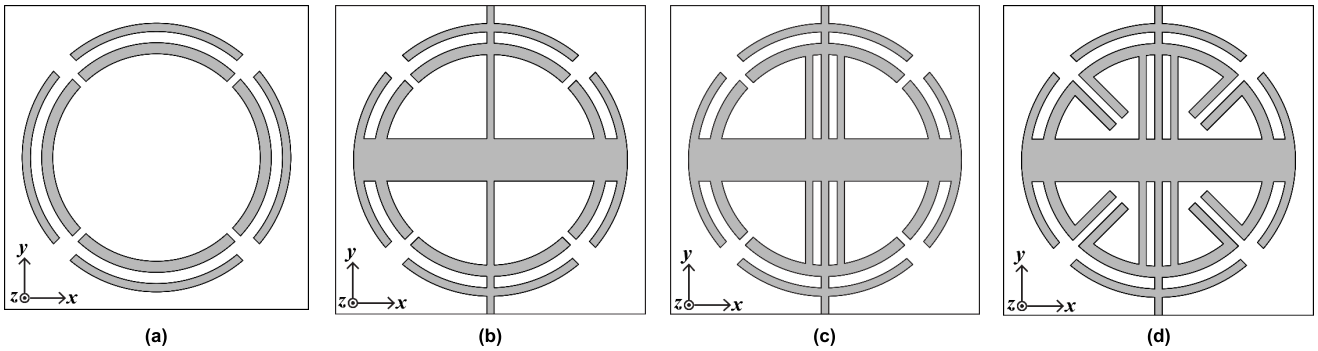

FIGURE 10. Design steps of the dual-band LTCP comprised of four parts (a) Type-I (b) Type-II (c) Type-III (d) Type-IV.

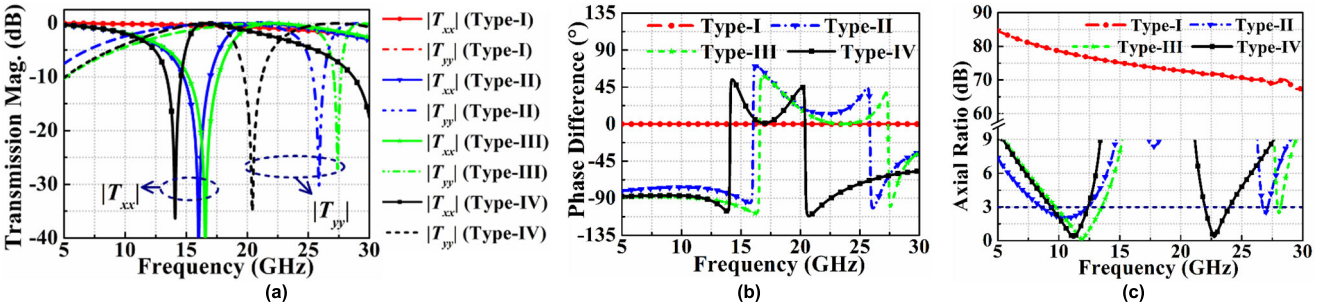

FIGURE 11. Simulated (a) co-polarized transmission magnitudes (b) phase difference between T_{xx} and T_{yy} (c) axial ratio of Type-I, Type-II, Type-III and Type-IV (proposed LTCP) unit cells.

The η_{CP} is > 94.2 % within the lower CP band, and the same is > 91.3 % within the higher CP band, as shown in Fig. 8. The surface current distribution on the designed metasurface at 11.2 and 22.75 GHz is presented in Fig. 9. For both x and y-incident wave, the maximum surface current can be seen on the CDR at the center frequency of the lower CP band, with negligible current on the CSRs. On the other hand, the circular rings exhibit maximum current at the center frequency of the higher CP band. This means by adjusting the values of the physical parameters it is possible to alter the frequency ratio between high to lower CP conversion bands.

F. DESIGN EVOLUTION OF THE DUAL-BAND LTCP

Fig. 10 shows the intermediate designed steps of the dual-band LTCP, which are Type-I, Type-II, Type-III and Type-IV metasurfaces. For each case, the simulated magnitude of co-polarized transmission coefficients ($|T_{xx}|$ and $|T_{yy}|$) and the phase difference between them are depicted in Fig. 11(a)-(b). The unit cell of the converter starts with a pair of concentric CSR resonators, where splits are symmetrically placed along the diagonal of each circular ring. The four-fold geometry of the dual CSRs allows similar transmission responses for x- and y-polarized incidence. The unit cell in Type-I enables a wideband transmission between 5-30 GHz with $|T_{xx}| = |T_{yy}| < -3$ dB and $\angle T_{xx}$-$\angle T_{yy} \approx 0°$ due to the isotropic nature of the unit cell, causing a high value of AR.

Fig. 11(c) presents the ARs of the unit cells in Type-I to Type-IV. The transmitted signal for Type-I is an LP wave with AR > 66.75 dB in the entire transmission band. The anisotropy in the Type-II metasurface is strategically introduced to obtain the circularly polarized transmitted wave. By including a metallic grid and dipole structure of asymmetric widths at the center of the unit cell, the required $\pm 90°$ phase difference between horizontal and vertical transmitted waves is achieved. This results in frequency-selective responses with TZs at 16 and 25.85 GHz for x and y-polarization. Notably, the common passbands for $|T_{xx}|$ and $|T_{yy}| > -3$ dB are observed within specific frequency ranges. In addition, the capacitive and inductive loading in Type-II metasurface induces phase delays and advancements for the horizontal and vertically polarized transmitted waves, impacting the AR to be below 3 dB at dual frequencies. The phase differences between the two co-polarized transmitted waves are $-76.8°$ and $-77.6°$ at 10.6 and 26.9 GHz, and magnitudes of $|T_{xx}|$ and $|T_{yy}|$ are nearly equal. The AR is obtained minimum with related values of 2.02 and 2.43 dB for Type-II metasurface. In the third step, a pair of vertical metal strips are added on each side of the wire grid. As the inductance of the vertical strips in parallel to the wire grid reduces the effective inductance for y-polarized incidence, the TZ of $|T_{yy}|$ shifts to a higher frequency. At the lower LP to CP conversion frequency, the phase difference between $\angle T_{xx}$ and $\angle T_{yy}$ becomes close to $-90°$ and the converter exhibits improved AR response. Finally, the Type-IV unit cell (proposed LTCP) incorporates parallel diagonal strips added to each split gap of the inner circular ring, enhancing

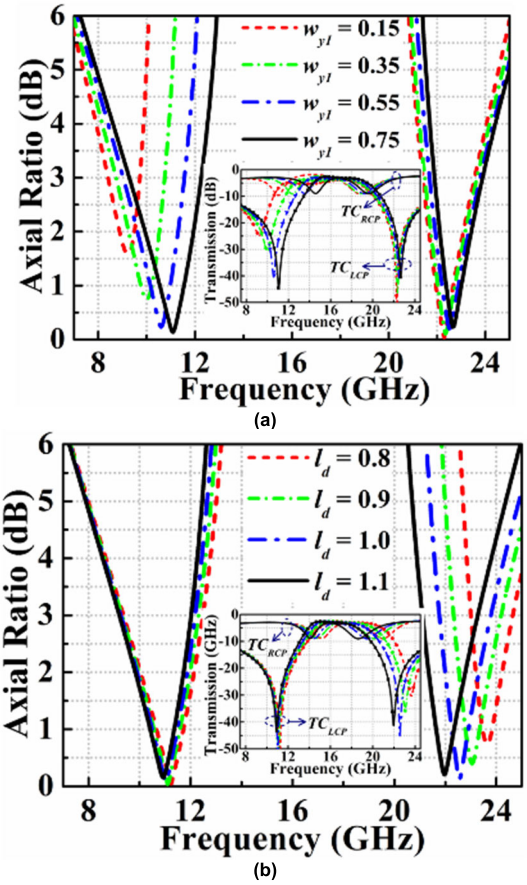

FIGURE 12. Parametric variation of the AR and circular transmission coefficients for different (a) widths (w_{y1}) of CDR (b) lengths (l_d) of the parallel diagonal strips attached to inner CSR.

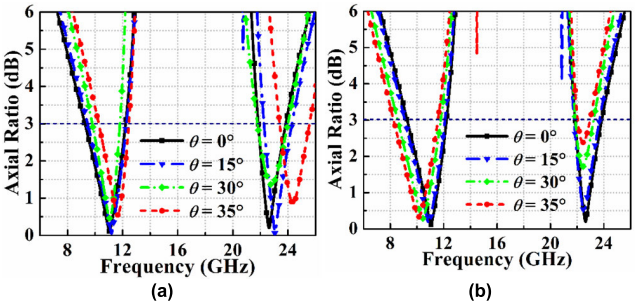

FIGURE 13. Simulated ARs at different incidence angles (a) *xz*-plane (b) *yz*-plane.

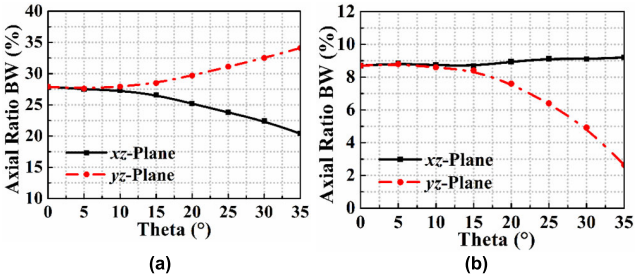

FIGURE 14. Simulated axial ratio bandwidth variation at different oblique angles for linear polarization to circular polarization conversion in (a) first band (b) second band.

capacitance and shifting the TZs to lower frequencies. The AR of the converter near the higher operating frequency has been improved; the reduced gradient of $\angle T_{xx}$ - $\angle T_{yy}$ at high frequency improves the LP to CP conversion BW.

It can be noted that due to center-connected geometry in the proposed dual-band LTCP, the structure exhibits low mutual coupling between the two orthogonal reflection and transmission components ($|R_{xy}|$ and $|T_{xy}|$) [28]. This causes cross-polarized reflection and transmission coefficients to be negligible, which is <-58 dB in simulation (not shown).

G. PARAMETRIC OPTIMIZATION AND ANGULAR STABILITY

One of the salient features of the proposed LTCP is the independent controllability of the two center frequencies. This was achieved by varying the width (w_{y1}) of CDR and length (l_d) of the diagonally oriented parallel strips, keeping all the remaining dimensions unaltered. Fig. 12 (a) shows that when the width w_{y1} of the dipole arm increased from 0.15 mm to 0.75 mm, the center frequency of the 1st CP band shifted from 9.2 to 11.1 GHz. This provides a tuning range of over 1.9 GHz for the lower center frequency, while minor effects can be seen on the 2nd band, causing a decrease in the frequency ratio between the two CP bands with an increase in w_{y1}. The higher frequency shift of the 1stCP band can be understood from the reduction of the inductance of the wide metal strip with an increase in w_{y1}. Similarly, the 2nd CP band can be altered by changing the l_d without affecting the 1st CP band (see Fig. 12(b)). The capacitance C_i of the inner circular ring increases with an increase in the l_d, causing a lower frequency shift of the 2nd CP band, hereby decreasing the frequency ratio between the two bands. The center frequency of the 2nd CP band can be altered over a range of 1.7 GHz from 21.95 to 23.65 GHz by changing the values of l_d. The inset of Fig. 12 also shows the variation of $|TC_{RCP}|$ and $|TC_{LCP}|$ with changes in w_{y1} and l_d. It is observed that the designed LTCP exhibits high co to cross-circular isolation over the tuning range of parameters. Fig. 13 presents ARs of the LTCP in two orthogonal planes (*xz* and *yz*) for different oblique angles (θ). The converter response is found stable up to an incidence angle of 35° in both planes with corresponding AR is $<$ 3 dB. The variation of AR BWs for the different values of θ is displayed in Fig. 14. The AR BW of the converter has changed in negligible amounts up to an incidence angle of 15° in both planes *xz* and *yz*. For the 1st LP to CP conversion band, AR BW decreases in the *xz* plane and increases in the *yz*-plane with an increase in θ. For the 2nd LP to CP conversion band, AR BW becomes stable in the *xz* plane even at a high oblique angle; but the AR BW decreases in the *yz* plane with an increase in θ. At the highest oblique angle, the minimum AR BW of the converter is achieved to be $>$ 20.4 % for the first CP band and $>$ 2.64 % for the second CP band.

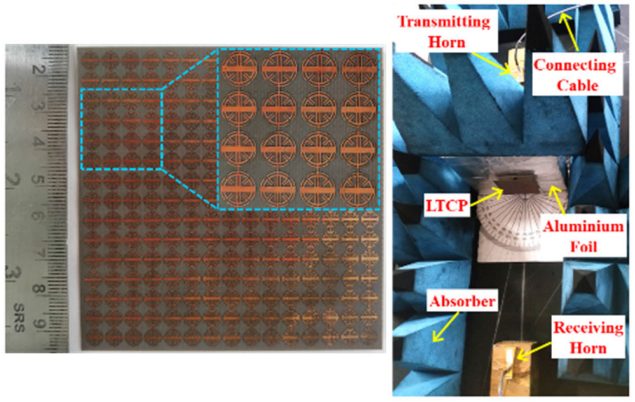

FIGURE 15. (a) Photographs of the fabricated dual-band LTCP (b) measurement setup to determine the AR of the converter.

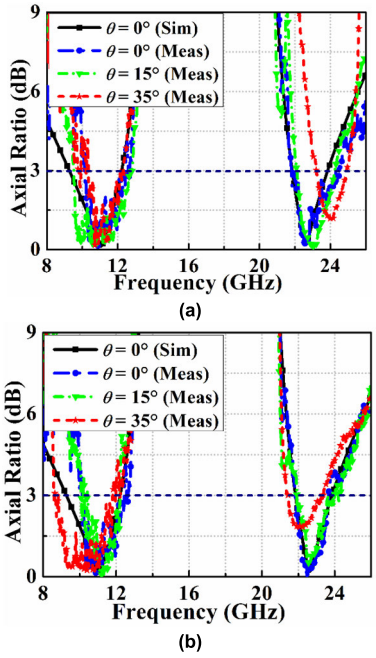

FIGURE 16. Measured ARs of the dual-band LTCP at normal and oblique angles (a) *xz*-plane (b) *yz*-plane.

III. MEASUREMENT RESULTS OF DESIGNED LTCP

An array of 15 × 15 elements of the designed dual-band LTCP was fabricated on a Taconic TLY-5 substrate using a standard PCB (printed circuit board) manufacturing process. Fig. 15 (a) depicts the 2D image of the converter's prototype, which has a lateral size of 81.75 × 81.75 mm^2. The experimental setup to measure the AR of the polarizer is shown in Fig. 15(b). The LTCP is placed between two broadband identical horn antennas (operating between 8 to 40 GHz), considered as transmitting (Tx) and receiving (Rx) antennas. The Tx and Rx horns are connected to a vector network analyzer (Model: Keysight N5224B) using coaxial cable. The spacing between the horns and converter is maintained above 35 cm or approximately $2D^2/\lambda$ to perform the transmission measurement in the far field. Here, D = 81.75 mm, and λ is the free space wavelength at the lowest frequency of the sweep. The gain of the horn at 11.2 and 22.75 GHz are 12.85 and 15.5 dBi, respectively.

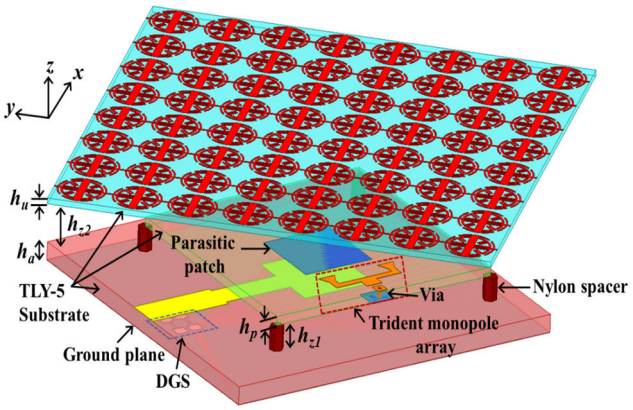

FIGURE 17. Isometric view of the proposed dual-band dual-orthogonal rotation CPMA using LTCP as a superstrate over dual-feed LPA.

The AR of the converter is measured at normal incidence and for different oblique incidences. The measurement was performed in two orthogonal planes (*xz* and *yz*) by rotating the converter surface by 90° around its vertical axis. Fig. 16 presents the measured AR of the polarizer, whose response is compared with the simulated AR at normal incidence. A satisfactory correlation is observed between the simulated and measured AR. The minor discrepancy, mainly at the lower CP band, can be seen, which is attributed to two reasons- (a) high impedance mismatch of the horn antenna near the cut-off frequency and (b) edge diffraction of the surface-wave at the converter's boundary. The scattering of the signal from the edges of the converter is partially reduced using aluminium foil and the microwave absorber. At normal incidence, the measured 3-dB AR BW is achieved between 10-12.54 GHz (22.5 %) in the lower CP band and between 21.82-24.57 GHz (11.8 %) in the higher CP band. The center frequencies of the two CP bands are measured at 10.9 and 22.5 GHz, with corresponding values of AR being 0.081 dB and 0.16 dB. In both the *xz* and *yz* planes, the converter shows stable AR performance up to an incident angle of 35°.

IV. DUAL BAND DUAL POLARIZED CP ANTENNAS

This section introduces a dual-band dual CP (RCP / LCP) antenna (array) system by integrating the LTCP with a dual-band dual-feed LP antenna (DF-LPA). Fig. 17 reveals the isometric view of the proposed CP antenna, where LTCP is placed as a superstrate over a DF-LPA. The LP antenna is rotated by an angle of 45° relative to the polarizer to generate the CP radiated wave. The antenna geometry, operating principle, simulation and measurement results are detailed in the following discussion.

A. ANTENNA GEOMETRY

This paper proposes a new dual-band dual orthogonal feed LP antenna with broadside radiation, operating in two

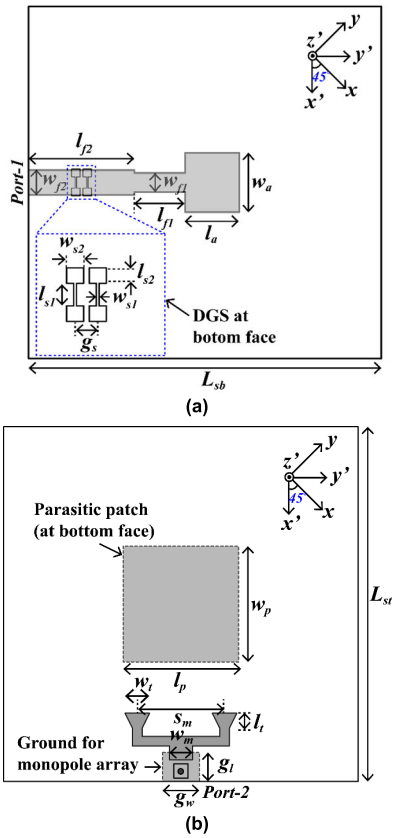

FIGURE 18. Schematic of the DF-LPA (a) DGS loaded microstrip antenna at the lower band (b) 2-element monopole array at the higher band with a parasitic patch on the backside of the coplanar dielectric.

non-adjacent bands - X and K of the microwave spectrum. The DF-LPA is realized using the concept of a shared ground plane. The metal ground at the bottom of the antenna is considered as a signal ground in the lower band and as a metallic reflector for the higher band. The architecture of the LP antenna consists of two dielectric substrates separated by a thin air spacer of height h_{z1} (see Fig. 17). The two substrates are of Taconic TLY-5 dielectric material and have heights of $h_a = 1.58$ mm and $h_p = 0.79$ mm. The geometry and corresponding physical dimensions of the DF-LPA are shown in Fig. 18, which shows the front views of the lower and upper substrates.

B. DUAL-BAND WORKING PRINCIPLE

The dual-band operation is achieved by integrating a radiating patch and a 2-element monopole array printed over stacked dielectric substrates. The lower frequency antenna is a conventional microstrip patch antenna (MPA) fed with a quarter wave transmission line. The radiating patch has a length $l_a = 7.68$ mm and width $w_a = 8.1$ mm. An additional rectangular patch (size of $l_p \times w_p = 7.45$ mm $\times$ 7.7 mm) is vertically placed over the radiating patch at a distance of $h_{z1} = 2$ mm to enhance the return loss BW. It can be shown that the reference microstrip antenna without a stacked radiating patch has an

TABLE 3. Geometrical parameters of LTCP loaded dual feed CP antenna.

l_a	w_a	l_{f1}	l_{f2}	w_{f1}	w_{f2}	l_{s1}	l_{s2}
7.68	8.1	7.2	8.5	2.68	3.5	1.6	1.1
w_{s1}	w_{s2}	g_s	l_p	w_p	l_t	w_t	s_m
0.2	1.21	1.61	7.45	7.7	1.1	1.8	6.6
w_m	g_l	g_w	h_{z1}	h_{z2}	L_{sb}	L_{st}	
1.7	2.12	2.7	2	11.8	35	24	

impedance BW of 5.9 % (10.93-11.6 GHz). For the designed antenna, the bottom rectangular patch acts as a driven patch, while the top patch acts as a parasitic patch, being electromagnetically coupled with the bottom patch. The parasitic patch is placed in the inverted configuration on the backside of the top TLY-5 substrate. The gap-coupled MPA resonates at two nearby frequencies, 10.2 and 11.55 GHz (see Fig. 19), showing an impedance matching over broadband, which exists in the lower LP to CP conversion band of LTCP. The 2nd radiating structure, made of 2-element monopole array, is optimized to resonate near the center frequency of the higher LP to CP conversion band. The array is printed on the front face of the top TLY-5 substrate. The array's elements are fed with a T-junction power divider. The monopole geometry is conceived in a trident pattern to improve its return loss BW. In a traditional configuration, the monopole array exhibits bi-directional radiation in the E-plane and omnidirectional radiation in the H-plane. In the DF-LPA architecture, the ground plane at the backface of the bottom TLY-5 substrate is conceived as a reflector to the monopole array to obtain uni-directional radiation in the broadside. Spacing between the reflector and monopole array is $\sim 0.26\ \lambda$, where 'λ' is the wavelength at the center frequency of the 2nd LP to CP conversion band. Since the resonance frequency of the monopole array is near the 1st harmonic of the rectangular patch antenna, it is required to suppress the harmonic to obtain polarization purity in the two orthogonal modes. A pair of dumbbell-shaped defected ground structures (DGS) is placed in the ground plane beneath the microstrip feed line to diminish the high-order harmonics of the radiating patch, as seen in Fig. 18(a). The suppression of high-order modes also eliminates undesired radiation with orthogonal polarization, causing good co to cross-polarized isolation in the radiation pattern [45]. The overall size of the DF-LPA is $35 \times 35 \times 4.4$ mm^3, which is $1.31 \times 1.31 \times 0.16\ \lambda_L^3$, with λ_L is the wavelength at 11.2 GHz. Table 3 shows the final dimensions of the dual-band antenna array.

C. SIMULATION RESULTS

Fig. 19(a) displays the simulated return losses of the DF-LPA when port-1 and port-2 are excited separately. It is noteworthy to mention that when one port of the LP antenna is excited, the remaining port is terminated with a 50 Ω broadband load. The dual-band LP antenna structure exhibits $|S_{11}| < -10$ dB from 9.78-12.22 GHz, having an impedance BW of 2.44 GHz or 22.2 %. Having excitation in port-1, the two resonances

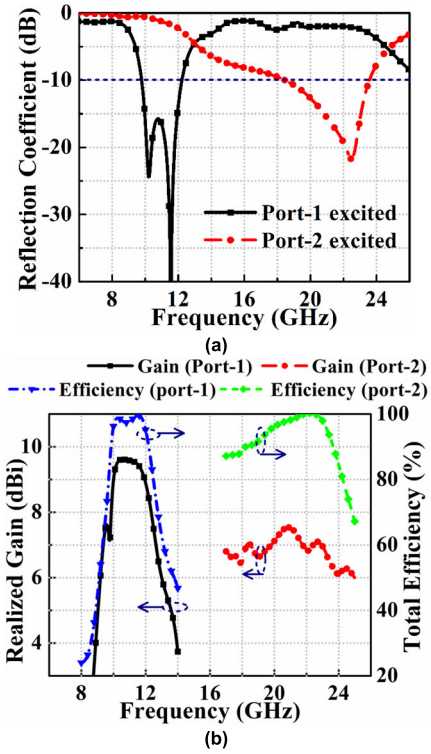

FIGURE 19. Simulated (a) reflection coefficients (b) gain and total efficiency variation of the DF-LPA with excitations to port-1 and port-2.

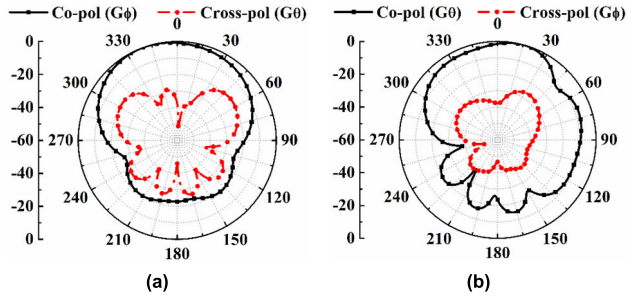

FIGURE 20. Simulated radiation pattern of the DF-LPA at 11.2 GHz with port-1 excited (a) x′ z′ -plane (b) y′ z′ -plane.

of the antenna exhibit return losses of 24.4 and > 40 dB, respectively. When the signal excitation is given at port-2, the DF-LPA resonates at 22.5 GHz with a return loss of 21.7 dB. The impedance BW of the antenna with $|S_{22}|$ <−10 dB covers frequencies between 18.46 to 23.57 GHz (5.11 GHz or 24.3 %). One can also notice that between the frequencies of 12.5 to 26 GHz, the high-order harmonics of the rectangular radiating patch have been suppressed. The gain and efficiency variation of the dual-band LP antenna are presented in Fig. 19(b). Within the return loss BWs, the gain of the DF-LPA varies between 7.2 to 9.6 dBi for the lower band and between 6.4 to 7.5 dBi for the higher band. The average efficiencies of the dual-band antenna are 96.8 % and 96.5 %, respectively.

Fig. 20 and Fig. 21 represent the 2D radiation patterns of the dual-band DF-LPA at the two operating frequencies of

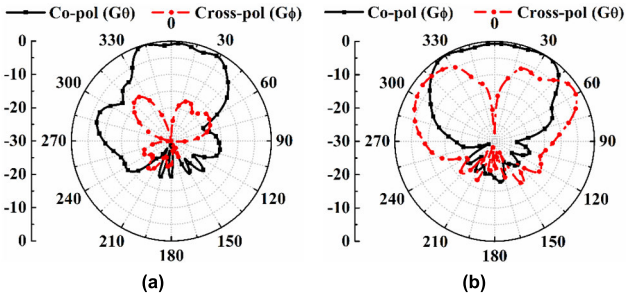

FIGURE 21. Simulated radiation pattern of the DF-LPA at 22.75 GHz with port-2 excited (a) x′ z′ -plane (b) y′ z′ -plane.

the LTCP. The DF-LPA radiates in the broadside direction in two principal planes- x' z' and y' z'. The front-to-back ratio of the dual-band antenna in the lower and higher operating frequencies is 14.6 and 13.8 dB, respectively. The antenna exhibits good co to cross-polarization (Xpol) discrimination along the broadside direction. In the x' z' and y' z' planes, the Xpol is achieved <−36.4 dB at the lower operating frequency and <−26.8 dB at the higher operating frequency.

D. EXPERIMENTAL RESULTS OF LTCP LOADED CPMA

Fig. 22(a)-(d) presents the photograph of the fabricated DF-LPA, depicting different metal layers printed on the front face and rear face of the lower and upper dielectric substrates. The two substrates are stacked together with an air-spacer of 2 mm between them. The photograph in Fig. 22(e) shows the final configuration of the dual-band LP antenna. The designed DF-LPA is combined with an LTCP converter, with feeds of the antenna rotated by 45° relative to the polarizer outer edges (see Fig. 18(f)-(g)). The air-spacer height (h_{z2}) between the DF-LPA and the converter is found through parametric optimization, and it's final value is 11.8 mm. The simulated and measured reflection coefficients of the converter-loaded DF-LPA are shown in Fig. 23. The measured $|S_{11}|$ and $|S_{22}|$ of the CP antenna is found to be well in accordance with the simulated response, except lower frequency shifts of the resonant frequencies and reduction of the return loss BW. This may be attributed to various factors like (a) error in the PCB prototype due to fabrication tolerance, (b) misalignment of the dielectric substrates during manual assemble of the multilayer architecture, (c) different array size (8 × 8) of the LTCP for simulating the CPMA (limited by computational resources) as compared to the measured prototype. With the excitation given to port-1 (while the port-2 is matched terminated with 50 Ω load resistance), the designed CP antenna exhibits 10 dB return loss BW from 10.47-12.62 GHz (18.6 %) in simulation and 10.21-12.25 GHz (18.2 %) in measurement. Conversely, when excitation is given to port-2, the CP antenna covers the BW of 19.83-22.85 GHz (14.2 %) in simulation and 20.78-22.4 GHz (7.5 %) in measurement.

Fig. 24 displays the simulated and measured transmission coefficients ($|S_{21}|$) of the dual-feed CPMA. The isolation between the ports is achieved > 24.8 and 35.1 dB at the center frequencies of the lower and higher return loss BWs. Fig. 25

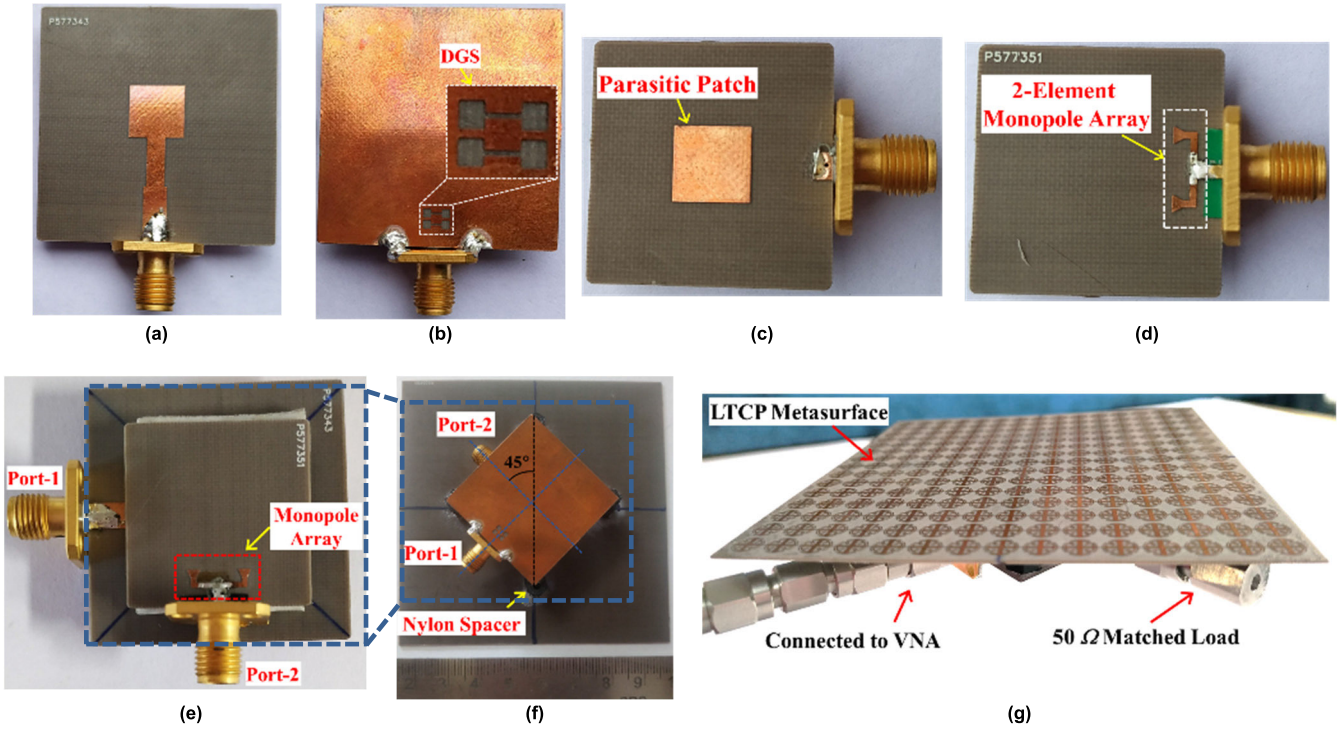

FIGURE 22. Fabricated prototype of the LTCP superstrate loaded DF-LPA. (a) and (b) the front and back views of the DGS-loaded microstrip antenna at the lower band. (c) and (d) back and front views of the monopole array with coplanar parasitic patch at higher band. (e) front view of the DF-LPA with two substrates stacked together. (f) and (g) back and 3D views of the dual-band dual orthogonal CPMA.

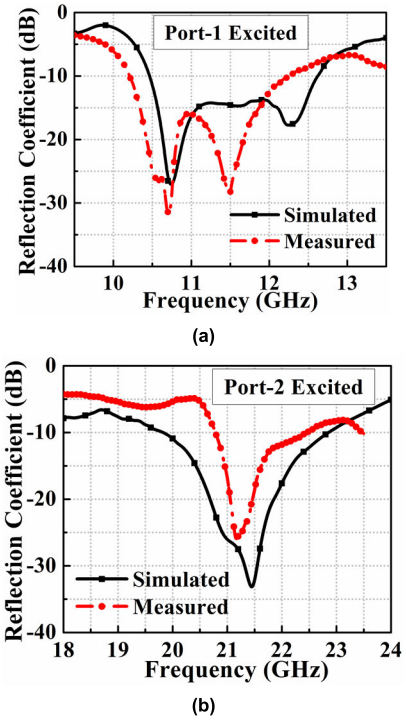

FIGURE 23. Simulated and measured reflection coefficients of the dual-band dual-feed CPMA for (a) port-1 excited (b) port-2 excited.

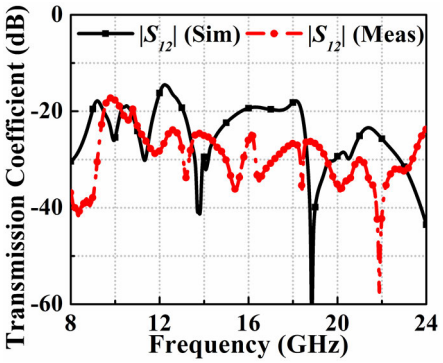

FIGURE 24. Simulated and measured isolation between the two ports of CPMA.

illustrates the AR of the proposed converter-loaded antenna in the lower and higher operating bands. In the first LP to CP band, the AR $\leq$ 3 dB is observed between 10.8-11.58 GHz (6.8 %) in the simulation and 10.9-11.5 GHz (5.4 %) in the measurement. For the 2nd band, the AR BW is obtained from 21.28-21.78 GHz (2.3 %) in simulation and 20.9-21.5 GHz (2.8 %) in measurement. These two AR BWs of the CPMA are seen to be much lower than the 3 dB AR BWs of the converter, which may be due to the non-zero cross-polarized radiation of the DF-LPA causing the amplitude imbalance in the two orthogonal transmitted waves from the metasurface.

E. RADIATION CHARACTERISTICS

The variation in gain of the dual-band CPMA for the lower and upper bands is exhibited in Fig. 26(a)-(b). With excitation

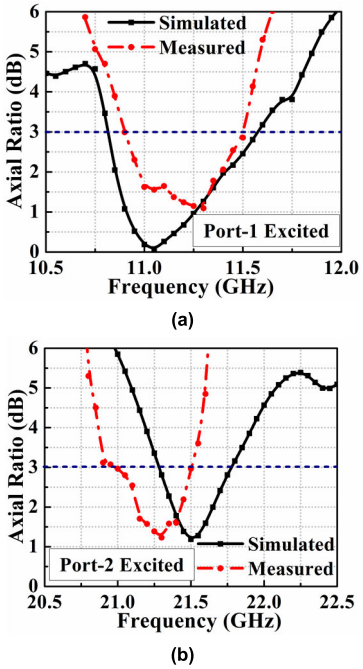

FIGURE 25. Simulated and measured ARs of the proposed dual-band CPMA in (a) lower band (b) higher band.

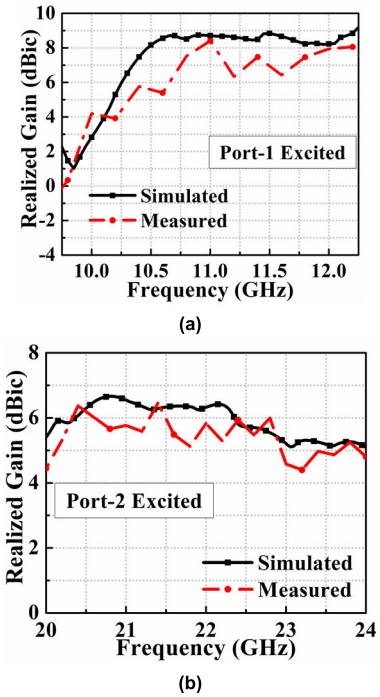

FIGURE 26. Simulated and measured gain characteristics of the proposed dual-band CPMA in (a) lower band (b) higher band.

at port-1, the measured gain has minimum and maximum values of 7.5 and 8.4 dBic within the AR BW, against simulated gain variation between 8.4 to 8.8 dBic. The gain of the antenna with excitation at port-2 is obtained between 6.25 to 6.36 dBic in simulation against that of 5.5 to 6.4 dBic in measurement. Fig. 27 and Fig. 28 show the simulated

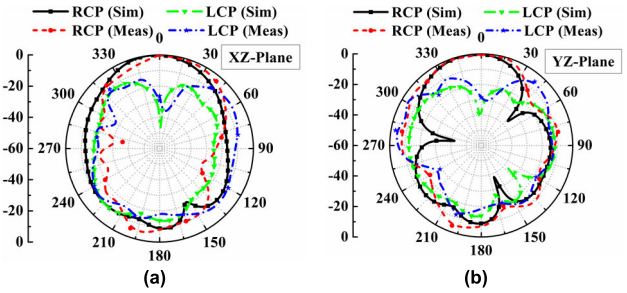

FIGURE 27. Simulated and measured radiation patterns of CPMA at 11.2 GHz (a) xz plane (b) yz plane.

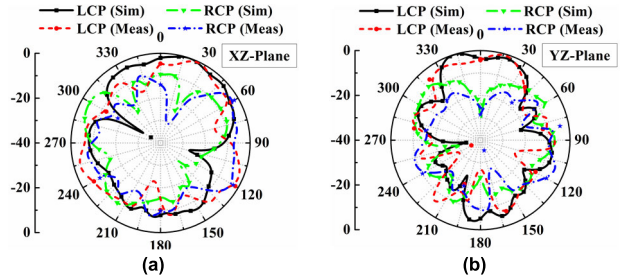

FIGURE 28. Simulated and measured radiation patterns of CPMA at 21.4 GHz (a) xz plane (b) yz plane.

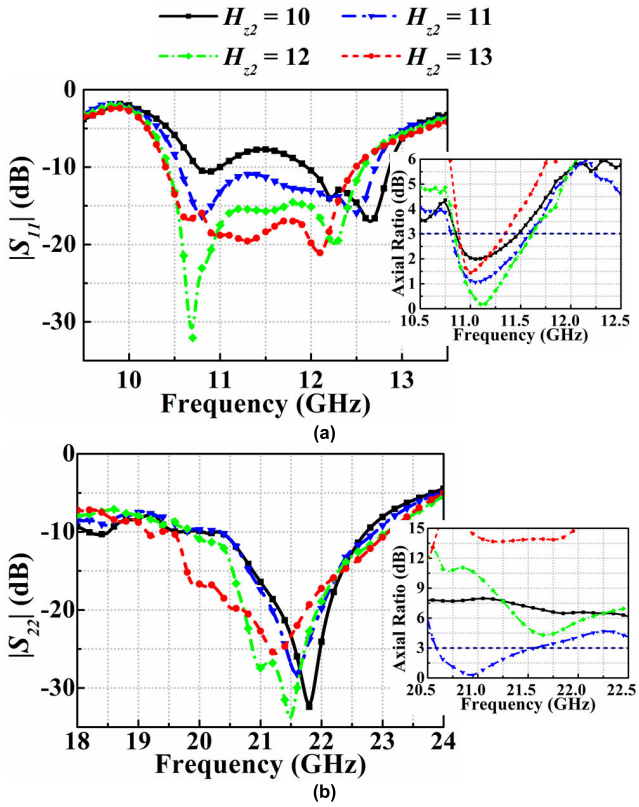

FIGURE 29. Simulated reflection coefficient and axial ratio of the converter loaded dual-feed CPMA at different heights of the air spacer (a) port-1 excited (b) port-2 excited.

and measured 2D radiation patterns of the CPMA in two orthogonal planes (*xz* and *yz*) at the center frequencies of

TABLE 4. Performance comparison of the designed linear to circular converter with previously reported work.

Ref.	Center Freq (GHz)	AR BW (%)	IL (dB)	Angle Stability	Cell Size (λ_L^2)	Thickness (λ_L)	FSS layer	Type	Polarization Mode	Controllability of Center Freq.
[19]	12.1, 17.7	6.6, 4.5	–	30°	3.9×8 mm^2 (0.051)	1.524 mm (0.061)	1	Reflective	Orthogonal	NR
[20]	35.95, 56.65	41.5, 17	–	45°	2×2 mm^2 (0.057)	0.8 mm (0.096)	1	Reflective	Orthogonal	NR
[28]	18.5, 29	29, 12	2, 0.8	20°	4×4 mm^2 (0.061)	1.575 mm (0.097)	2	Transmissive	Orthogonal	NR
[29]	20.67, 29.71	5.56, 3.97	1.25, 1	45° (sim)	3.9×3.72 mm^2 (0.069)	60 mil (0.105)	2	Transmissive	Orthogonal	NR
[30]	17.8, 36.5	25, 16.4			5.2×5.2 mm^2 (0.095)	0.3 mm (0.018)	2	Transmissive	Orthogonal	NR
[31]	19.3, 29.35	21.8, 12.6	0.5, 0.6	45°	2.6×3 mm^2 (0.032)	1.5 mm (0.096)	2	Transmissive	Orthogonal	Partially
[32]	19.95, 29.75	5.6, 8.3	0.1, 0.6	45°	5.3×5.3 mm^2 (0.124)	1.05 mm (0.069)	3	Transmissive	Orthogonal	NR
[33]	20.1, 29.55	20.8, 5.8	1, 1	45°	2.8×2.8 mm^2 (0.035)	3.048 mm (0.204)	3	Transmissive	Orthogonal	NR
[34]	7.6, 13	31.6, 13.8	1.5, 1.5	25°	9.22×8.8 mm^2 (0.052)	9.62 mm (0.24)	4	Transmissive	Same	NR
[35]	2.4, 5.8	15.8, 12.6	~ 2, 2	45°	33.3×32 mm^2 (0.068)	0.8 mm (0.0064)	1	Transmissive	Same	NR
Proposed LTCP	10.9, 22.5	22.5, 11.8	2.91, 2.96	35°	5.45×5.45 mm^2 (0.039)	0.51 mm (0.018)	1	Transmissive	Same	Yes

lower and high bands. The measured patterns are found to be consistent with the simulated result, having orthogonal circular polarization at two frequencies. In the lower frequency, the maximum radiation of the CPMA is seen in the broadside direction, with the difference of RCP to LCP patterns is $>$ 14.9 dB. For higher frequency, maximum radiation is tilted at an angle of 23.4° relative to broadside direction, having the difference of LCP to RCP is $>$ 15.9 dB. At the higher band, the tilt in the CP radiation pattern arises due to the asymmetric location of the monopole array relative to the co-planar parasitic patch at the bottom layer. Alongside the bottom ground plane, the parasitic patch also reflects the radiation of the monopole array in the off-set direction.

F. EFFECTS OF AIR SPACER HEIGHT

The effect of changing the air-spacer height between LTCP and LPA is further analyzed in Fig. 29. One can notice that the return loss BW and AR of the CPMA are affected by changes in h_{z2}, especially for excitation at port-2. The AR at the 2nd band increases to a high value when the value of h_{z2} is $>$ 12 mm. This is because of the tilt in the radiation pattern at the higher band, causing an oblique incidence on the polarization converter. When the metasurface is far away from the feed, the radiation from the LPA cannot adequately illuminate the metasurface, as most of the waves has been scattered from the edges of the converter. This causes the transmitted wave to be elliptically polarized instead of circular polarized, increasing the value of AR.

The performance of the designed transmissive type LTCP is compared with other dual-band circular polarizers in Table 4. The designed converter is noted to have a smaller unit cell size except [31] and [33]. Although the single-layer converters, as reported in [20] and [35] exhibit higher angular stability than the present work, but their unit cell size is much higher than this work. The profile height of the designed LTCP is found to be among the minimum, confirming its ultrathin characteristic. Unlike other unit cells, one of the major advantages of the suggested structure is the independent wideband tuning of the LP-to-CP conversion frequencies.

V. CONCLUSION

This paper presents a new single-layer, transmissive LP-to-CP converter with wide AR BWs at two non-adjacent frequencies. The converter response is analyzed with the corresponding circuit model and further validated with full-wave simulation and measurement results. The converter exhibits an oblique angle stability of 35° for AR is lower than 3 dB over the bands of 10-12.54 GHz and 21.82-24.57 GHz. The designed LTCP is included as a superstrate over a dual-band DF-LPA to generate orthogonal CP waves (RCP/LCP) at two frequencies. The measured AR BWs of the proposed CPMAs are 5.4 and 2.8 %, with a peak gain of 8.4 and 6.4 dBic, respectively. The designed CPMA has potential applications in X / K-band SatCom, synthetic aperture radars (SAR), and multiband wireless systems.

ACKNOWLEDGMENT

One of the authors appreciates the support received from the Department of Science and Technology, Government of India, and also acknowledge the IEEE Antenna Propagation Society for the 2023 APSF Fellowship.

REFERENCES

[1] Q.-W. Lin, S. Alkaraki, H. Wong, and J. R. Kelly, "A wide-band circularly polarized antenna based on anisotropic metamaterial," *IEEE Trans. Antennas Propag.*, vol. 71, no. 2, pp. 1254–1262, Feb. 2023.

[2] M. Dvorsky, M. T. A. Qaseer, and R. Zoughi, "Polarimetric synthetic aperture radar imaging with radially polarized antennas," *IEEE Trans. Instrum. Meas.*, vol. 69, no. 12, pp. 9866–9879, Dec. 2020.

[3] J. T. S. Sumantyo, M. Y. Chua, C. E. Santosa, G. F. Panggabean, T. Watanabe, B. Setiadi, F. D. S. Sumantyo, K. Tsushima, K. Sasmita, A. Mardiyanto, and E. Supartono, "Airborne circularly polarized synthetic aperture radar," *IEEE J. Sel. Topics Appl. Earth Observ. Remote Sens.*, vol. 14, pp. 1676–1692, 2021.

[4] W. Yang, J. Zhou, Z. Yu, and L. Li, "Single-fed low profile broadband circularly polarized stacked patch antenna," *IEEE Trans. Antennas Propag.*, vol. 62, no. 10, pp. 5406–5410, Oct. 2014.

[5] K. Ding, C. Gao, D. Qu, and Q. Yin, "Compact broadband circularly polarized antenna with parasitic patches," *IEEE Trans. Antennas Propag.*, vol. 65, no. 9, pp. 4854–4857, Sep. 2017.

[6] Y. Xu, H. Hu, B. Chen, M. Chen, J. Tian, and S. Lei, "Broadband high gain circularly polarized antenna for conformal applications," *IEEE Antennas Wireless Propag. Lett.*, vol. 22, no. 8, pp. 2032–2036, Aug. 2023, doi: 10.1109/LAWP.2023.3272485.

[7] C.-F. Liang, Y.-P. Lyu, D. Chen, W. Zhang, and C.-H. Cheng, "A low-profile and wideband circularly polarized patch antenna based on TM11 and TM21," *IEEE Trans. Antennas Propag.*, vol. 69, no. 8, pp. 4439–4446, Aug. 2021.

[8] Y.-J. Hu, W.-P. Ding, and W.-Q. Cao, "Broadband circularly polarized microstrip antenna array using sequentially rotated technique," *IEEE Antennas Wireless Propag. Lett.*, vol. 10, pp. 1358–1361, 2011.

[9] X. Quan, R. Li, and M. M. Tentzeris, "A broadband omnidirectional circularly polarized antenna," *IEEE Trans. Antennas Propag.*, vol. 61, no. 5, pp. 2363–2370, May 2013.

[10] J.-H. Lu and S.-F. Wang, "Planar broadband circularly polarized antenna with square slot for UHF RFID reader," *IEEE Trans. Antennas Propag.*, vol. 61, no. 1, pp. 45–53, Jan. 2013.

[11] L. Wang, W.-X. Fang, Y.-F. En, Y. Huang, W.-H. Shao, and B. Yao, "Wide-band circularly polarized cross-dipole antenna with parasitic elements," *IEEE Access*, vol. 7, pp. 35097–35102, 2019.

[12] X. Li, R. Ma, H. Cai, Y.-M. Pan, and X. Y. Zhang, "High-gain dual-band aperture-shared CP patch antenna with wide AR beamwidth for satellite navigation system," *IEEE Antennas Wireless Propag. Lett.*, vol. 22, no. 8, pp. 1888–1891, Aug. 2023, doi: 10.1109/LAWP.2023.3268653.

[13] C. Sun, H. Zheng, and Y. Liu, "Analysis and design of a low-cost dual-band compact circularly polarized antenna for GPS application," *IEEE Trans. Antennas Propag.*, vol. 64, no. 1, pp. 365–370, Jan. 2016.

[14] X. Qing and Z. N. Chen, "A compact dual-band circularly polarized antenna for satellite systems," in *Proc. IEEE Region Conf.*, Penang, Malaysia, Nov. 2017, pp. 2374–2377.

[15] T. Yue, Z. H. Jiang, and D. H. Werner, "A compact metasurface-enabled dual-band dual-circularly polarized antenna loaded with complementary split ring resonators," *IEEE Trans. Antennas Propag.*, vol. 67, no. 2, pp. 794–803, Feb. 2019.

[16] E. Martinez-de-Rioja, J. A. Encinar, A. Pino, and Y. Rodriguez-Vaqueiro, "Broadband linear-to-circular polarizing reflector for space applications in Ka-band," *IEEE Trans. Antennas Propag.*, vol. 68, no. 9, pp. 6826–6831, Sep. 2020.

[17] W. Chaihongsa, R. Kuse, K. Furuya, C. Phongcharoenpanich, and T. Fukusako, "Broadband linear-to-circular polarisation conversion using the diamond-shaped reflecting metasurface," *IET Microw., Antennas Propag.*, vol. 14, no. 9, pp. 943–949, May 2020.

[18] S. Li and X. Zhang, "An ultra-wideband linear-to-circular polarization converter in reflection mode at terahertz frequencies," *Microw. Opt. Technol. Lett.*, vol. 61, no. 12, pp. 2675–2680, Dec. 2019.

[19] W. Tang, S. Mercader-Pellicer, G. Goussetis, H. Legay, and N. J. G. Fonseca, "Low-profile compact dual-band unit cell for polarizing surfaces operating in orthogonal polarizations," *IEEE Trans. Antennas Propag.*, vol. 65, no. 3, pp. 1472–1477, Mar. 2017.

[20] X. Liu, Y. Zhou, C. Wang, L. Gan, X. Yang, and L. Sun, "Dual-band dual-rotational-direction angular stable linear-to-circular polarization converter," *IEEE Trans. Antennas Propag.*, vol. 70, no. 7, pp. 6054–6059, Jul. 2022.

[21] S. M. A. Momeni Hasan Abadi and N. Behdad, "Wideband linear-to-circular polarization converters based on miniaturized-element frequency selective surfaces," *IEEE Trans. Antennas Propag.*, vol. 64, no. 2, pp. 525–534, Feb. 2016.

[22] E. Arnieri, F. Greco, and G. Amendola, "A broadband, wide-angle scanning, linear-to-circular polarization converter based on standard Jerusalem cross frequency selective surfaces," *IEEE Trans. Antennas Propag.*, vol. 69, no. 1, pp. 578–583, Jan. 2021.

[23] W. Zhang, J.-Y. Li, and J. Xie, "A broadband circular polarizer based on cross-shaped composite frequency selective surfaces," *IEEE Trans. Antennas Propag.*, vol. 65, no. 10, pp. 5623–5627, Oct. 2017.

[24] F. Zhang, G.-M. Yang, and Y.-Q. Jin, "Design and analysis of linear to circular polarization converter with third-order meta-frequency selective surfaces," *IEEE Trans. Antennas Propag.*, vol. 68, no. 9, pp. 6646–6655, Sep. 2020.

[25] J. D. Baena, S. B. Glybovski, J. P. del Risco, A. P. Slobozhanyuk, and P. A. Belov, "Broadband and thin linear-to-circular polarizers based on self-complementary zigzag metasurfaces," *IEEE Trans. Antennas Propag.*, vol. 65, no. 8, pp. 4124–4133, Aug. 2017.

[26] H. B. Wang, Y. J. Cheng, and Z. N. Chen, "Wideband and wide-angle single-layered-substrate linear-to-circular polarization metasurface converter," *IEEE Trans. Antennas Propag.*, vol. 68, no. 2, pp. 1186–1191, Feb. 2020.

[27] S. Dey and S. Dey, "Broadband single layer transmission type linear to circular polarization converter with higher conversion efficiency," in *Proc. IEEE 19th Int. Symp. Antenna Technol. Appl. Electromagn. (ANTEM)*, Winnipeg, MB, Canada, Aug. 2021, pp. 1–2.

[28] H. B. Wang and Y. J. Cheng, "Single-layer dual-band linear-to-circular polarization converter with wide axial ratio bandwidth and different polarization modes," *IEEE Trans. Antennas Propag.*, vol. 67, no. 6, pp. 4296–4301, Jun. 2019.

[29] M. A. Sofi, K. Saurav, and S. K. Koul, "Frequency-selective surface-based compact single substrate layer dual-band transmission-type linear-to-circular polarization converter," *IEEE Trans. Microw. Theory Techn.*, vol. 68, no. 10, pp. 4138–4149, Oct. 2020.

[30] A. K. Fahad, C. Ruan, R. Nazir, T. U. Haq, and W. He, "Dual-band ultrathin meta-array for polarization conversion in Ku/Ka-band with broadband transmission," *IEEE Antennas Wireless Propag. Lett.*, vol. 19, pp. 856–860, 2020.

[31] Y. Chen, G. Zhai, S. Wang, J. Gao, and J. Ren, "Dual-band single-layered linear-to-dual-circular polarization converter with high angle stability for satellite communication," *IEEE Antennas Wireless Propag. Lett.*, vol. 22, no. 8, pp. 2017–2021, Aug. 2023.

[32] P. Naseri, S. A. Matos, J. R. Costa, C. A. Fernandes, and N. J. G. Fonseca, "Dual-band dual-linear-to-circular polarization converter in transmission mode application to K/Ka-band satellite communications," *IEEE Trans. Antennas Propag.*, vol. 66, no. 12, pp. 7128–7137, Dec. 2018.

[33] M. Del Mastro, M. Ettorre, and A. Grbic, "Dual-band, orthogonally-polarized LP-to-CP converter for SatCom applications," *IEEE Trans. Antennas Propag.*, vol. 68, no. 9, pp. 6764–6776, Sep. 2020.

[34] Q. Zeng, W. Ren, H. Zhao, Z. Xue, and W. Li, "Dual-band transmission-type circular polariser based on frequency selective surfaces," *IET Microw., Antennas Propag.*, vol. 13, no. 2, pp. 216–222, Jan. 2019.

[35] T.-L. Vu and C. Seo, "A high angular stability, single-layer transmission linear-to-circular polarization converter for dual ISM-band operation," *IEEE Access*, vol. 11, pp. 30188–30196, 2023.

[36] C. Fu, L. Zhang, X. Zhang, W. Yu, S. Dong, X. Liu, and L. Han, "A tunable dual-band flexible polarization converter based on vanadium dioxide reflective metasurface," *Phys. Status Solidi (A)*, vol. 221, no. 3, Feb. 2024, Art. no. 2300291.

[37] X. Yuan, J. Chen, J. Wu, X. Yan, Y. Zhang, and X. Zhang, "Graphene-based tunable linear and linear-to-circular polarization converters in the THz band," *Results Phys.*, vol. 37, Jun. 2022, Art. no. 105571.

[38] F. Qin, S. S. Gao, Q. Luo, C.-X. Mao, C. Gu, G. Wei, J. Xu, J. Li, C. Wu, K. Zheng, and S. Zheng, "A simple low-cost shared-aperture dual-band dual-polarized high-gain antenna for synthetic aperture radars," *IEEE Trans. Antennas Propag.*, vol. 64, no. 7, pp. 2914–2922, Jul. 2016.

[39] M. Li, B. G. Zhong, and S. W. Cheung, "Isolation enhancement for MIMO patch antennas using near-field resonators as coupling-mode transducers," *IEEE Trans. Antennas Propag.*, vol. 67, no. 2, pp. 755–764, Feb. 2019.

[40] S. Dey and S. Dey, "Miniaturized near all angle stable 2.5D FSS for dual band shielding in transmission mode and multiband absorption in reflection mode," *IEEE Trans. Antennas Propag.*, vol. 71, no. 9, pp. 7323–7332, Sep. 2023.

[41] A. Elhawil, J. Stiens, C. De Tandt, W. Ranson, and R. Vounckx, "An equivalent circuit model of single circular open-ring resonators," *IEEE J. Sel. Topics Quantum Electron.*, vol. 16, no. 2, pp. 380–385, Mar./Apr. 2010.

[42] K. Sarabandi and N. Behdad, "A frequency selective surface with miniaturized elements," *IEEE Trans. Antennas Propag.*, vol. 55, no. 5, pp. 1239–1245, May 2007.

[43] Y. Hou, C. Zhang, and C. Wang, "High-efficiency and tunable terahertz linear-to-circular polarization converters based on all-dielectric metasurfaces," *IEEE Access*, vol. 8, pp. 140303–140309, 2020.

[44] J.-M. Xie, B. Li, and L. Zhu, "Dual-band circular polarizers with versatile polarization conversions based on aperture-coupled patch resonators," *IEEE Trans. Antennas Propag.*, vol. 70, no. 7, pp. 5584–5596, Jul. 2022.
[45] C. Sarkar, D. Guha, C. Kumar, and Y. M. M. Antar, "New insight and design strategy to optimize cross-polarized radiations of microstrip patch over full bandwidth by probe current control," *IEEE Trans. Antennas Propag.*, vol. 66, no. 8, pp. 3902–3909, Aug. 2018.

SOUMIK DEY (Graduate Student Member, IEEE) received the B.Sc. degree (Hons.) in physics from the Ramakrishna Mission Residential College, Narendrapur, in 2012, and the B.Tech. and M.Tech. degrees in radio physics and electronics from the University of Calcutta, in 2016 and 2018, respectively. He is currently pursuing the Ph.D. degree with the Department of Electrical Engineering, Indian Institute of Technology Palakkad (IIT Palakkad), India. From December 2018 to June 2019, he was a Research Staff at IIT Palakkad before transitioning to the Ph.D. program, in July 2019. He has published more than 40 research papers in several international journals and conferences and filed three Indian patents. His current research interests include broadband and multiband antennas, frequency-selective surface, metamaterial, electromagnetic bandgap structure, MIMO antennas, phased array, passive beamforming networks, and substrate-integrated waveguides. He was a recipient of the DST Inspire Fellowship (IF190116) from the Government of India and the IEEE Antennas and Propagation Society Fellowship (APSF), in 2023. He also achieved the first rank in the university's M.Tech. program. Furthermore, he held positions as the Vice Chair and the Chair of the IEEE AP-S Student Branch Chapter of IIT Palakkad, from 2022 to 2023. He has actively participated in scholarly endeavors as a reviewer for multiple journals, including the *International Journal of Antennas and Propagation*, *Scientific Reports* (Nature), and IEEE Open Journal of Antennas and Propagation, and conferences, such as AP-S URSI 2022.

SUKOMAL DEY (Senior Member, IEEE) received the B.Tech. degree in electronics and communication engineering from West Bengal University of Technology, Kolkata, India, in 2006, the M.Tech. degree in mechatronics engineering from Indian Institute of Engineering Science and Technology (IIEST), Shibpur, India, in 2008, and the Ph.D. degree from the Centre for Applied Research in Electronics (CARE), Indian Institute of Technology Delhi, in July 2015.

From August 2015 to July 2016, he was a Project Scientist with the Industrial Research and Development Centre, IIT Delhi. From August 2016 to June 2018, he was with the Radio Frequency Microsystem Laboratory, National Tsing Hua University, Taiwan, as a Postdoctoral Research Fellow. From June 2018 to June 2023, he was an Assistant Professor with the Department of Electrical Engineering, Indian Institute of Technology Palakkad, Kerala, India, where he has been an Associate Professor, since June 2023. He also worked on a collaborative research project supported by Synergy Microwave Corporation, Paterson, NJ, USA. He has authored or coauthored more than 150 research papers, three state-of-the-art books, three book chapters, and filed 17 patents. His research interests include electromagnetic metamaterial structures, frequency-selective surfaces, microwave imaging, and microwave-integrated circuits, including antennas and RFMEMS. He was a recipient of the Postgraduate Student Award from the Institute of Smart Structure and System, Bengaluru, in 2012; the Best Industry Relevant Ph.D. Thesis Award from the Foundation for Innovation in Technology Transfer, IIT Delhi, in 2016; the Distinction in Doctoral Research from IIT Delhi, in 2016; the Postdoctoral Fellow Scholarships from the Ministry of Science and Technology (MOST), Taiwan, in 2016 and 2017; the Early Career Research Award (ECRA) from the Science and Engineering Research Board (SERB), Government of India, in 2019; the Smt. Ranjana Pal Memorial Award from the Institution of Electronics and Communication Engineers (IETE), in 2021; the Technology Translation Award from the SERB, India, in 2023; and several best paper awards with his students from national and international IEEE conferences. He has been inducted into the technical program committees 4 and 6 of the IEEE MTT Society. He is a fellow of IETE, India, and current Chairperson of the IEEE Antenna and Propagation Society, Kerala Chapter, India.